Dynamic symmetry breaking and spin splitting in metal halide perovskites

Scott McKechnie,[1] Jarvist M. Frost,[2] Dimitar Pashov,[1] Pooya Azarhoosh,[1] Aron Walsh,[2,3,*] and Mark van Schilfgaarde[1,†]
[1]*Department of Physics, King's College London, London WC2R 2LS, United Kingdom*
[2]*Department of Materials, Imperial College London, London SW7 2BZ, United Kingdom*
[3]*Department of Materials Science and Engineering, Yonsei University, Seoul 03722, Korea*

(Received 29 October 2017; revised manuscript received 10 July 2018; published 6 August 2018)

Metal halide perovskites exhibit a materials physics that is distinct from traditional semiconductors. While materials such as $CH_3NH_3PbI_3$ are nonmagnetic, the presence of heavy elements (Pb and I) in a noncentrosymmetric crystal environment result in a spin splitting of the frontier electronic bands through the Rashba-Dresselhaus effect. We show, from a combination of *ab initio* molecular dynamics, density-functional theory, and quasiparticle *GW* theory, that the nature (magnitude and orientation) of the band splitting depends on the local asymmetry around the Pb and I sites in the perovskite structure. The potential fluctuations vary in time as a result of thermal disorder. We show that the same physics emerges both for the organic-inorganic $CH_3NH_3PbI_3$ and the inorganic $CsPbI_3$ compound. The results are relevant to the photophysics of these compounds and are expected to be general to other lead iodide containing perovskites.

DOI: 10.1103/PhysRevB.98.085108

I. INTRODUCTION

In crystals that preserve both time-reversal and spatial-inversion symmetry, there is at least a double degeneracy of the electron energy bands $E_n(k)$ for each wave vector k in the Brillouin zone [1]. However, the removal of spatial inversion symmetry produces an asymmetric potential, which, through the spin-orbit interaction, lifts the twofold spin degeneracy [2]. Dresselhaus and Rashba were the first to provide group theory descriptions of the effect of spin-orbit coupling (SOC) on noncentrosymmetric zincblende [3] and wurtzite [4–6] structures [7]. In a later work, Bychkov and Rashba pointed out that the analysis also applied to 2D systems [8]. The so-called Rashba effect is associated with a spin splitting of the dispersion $E(k)$ that is linear in k and a spin texture that is helical [2,5,9]. On the other hand, the Dresselhaus effect typically displays a splitting that is cubic in k and a nonhelical spin texture [2,3,9]. A recent study by Zunger *et al.* [10] provides a concise definition of the Rashba and Dresselhaus splittings, emphasizing the local origin of these effects: Atomic sites without inversion symmetry can either be polar (local Rashba) or nonpolar (local Dresselhaus) and the bulk effect is a vector sum over all sites (allowing for the coexistence of bulk Rashba and bulk Dresselhaus). Both are rooted in spin-orbit interactions at sites with local asymmetry and result in spin-split bands; from here on, 'spin splitting' will be used as a collective term for the two effects.

Spin splitting is now seen as a crucial feature in the electronic structure of solid-state systems. Indeed, exploiting these effects to control the electron spin is a central goal in spintronics [11,12]. It is also emerging as an important aspect of materials for photovoltaics, where it is thought to strongly influence the absorption and transport properties in perovskite solar cells [13–23]. Metal halide perovskites have attracted significant attention for solar-energy conversion, with champion light-to-electricity conversion efficiencies exceeding 22% for laboratory scale devices [24,25]. The unique physics of these materials is also extending their range of applications to areas including light-emitting diodes, spintronics, and solid-state sensors [26,27].

The archetype material, $CH_3NH_3PbI_3$ (or $MAPbI_3$), is composed of corner-sharing lead-iodide octahedra, with a charge-balancing organic cation in the void regions, forming a three-dimensional perovskite structure. With the large nuclear charges of lead and iodine, the electron kinetic energies near these cores are large. Relativistic effects become important. These materials also exhibit reduced symmetry resulting in local asymmetry which, through the Rashba and Dresselhaus effects, can split the bands into separate spin channels and shift the location of valence and conduction band extrema. This can lead to spin and momentum forbidden transitions that suppress electron-hole recombination [16,17,28]. First-principles electronic-structure calculations predicted that such relativistic effects could result in a direct to indirect band-gap transition in Pb-based perovskites [13–17,29]. There are increasing data to support this hypothesis. Indirect transitions are implicated for the observed slow minority carrier recombination [20–23]. In particular, angle-resolved x-ray photoemission spectroscopy (ARPES) has been used to directly resolve indirect features in the band structure [21].

In this work, we study the effect of local symmetry breaking (arising both statically and dynamically) on the electronic structure of lead halide perovskites. We sample structures from finite-temperature molecular dynamic simulations and evaluate the spin splitting. The band splitting directly impacts the photophysics of an operating solar cell, and it is also a relevant metric of local asymmetry. By making identical studies of both organic-cation and inorganic perovskites, we show

*a.walsh@imperial.ac.uk
†mark.van_schilfgaarde@kcl.ac.uk

TABLE I. Band gaps (E_g) and band splittings (E_R and k_0) for a range of halide perovskites calculated for static (athermal) structures including scalar-relativistic effects and spin-orbit coupling (SOC) where stated. Splittings are shown for both the valence band (VB) and the conduction band (CB). Measured band gaps, E_g^{EXP}, are also shown. The structural model for each perovskite is indicated by the prefix o (orthorhombic); t (tetragonal); pc (pseudocubic); c (cubic).

				QS*GW*			
Material	E_g (eV)	E_g^{SOC}	E_g^{EXP}	${E_R}^{\mathrm{CB}}$ (meV)	${E_R}^{\mathrm{VB}}$	${k_0}^{\mathrm{CB}}$ (Å^{-1})	${k_0}^{\mathrm{VB}}$
o- $MAPbI_3$	2.63	1.84	1.65 [37]	0	0	0	0
t- $MAPbI_3$	2.67	1.99	1.61 [37]	10	2	0.025	0.010
pc- $MAPbI_3$	2.72	1.87	1.63 [38]	82	10	0.060	0.029
pc- $FAPbI_3$	2.52	1.61	1.52 [37]	28	1	0.030	0.009
pc- $CsPbI_3$	2.81	1.95		87	8	0.062	0.031
c- $CsPbI_3$	2.48	1.51	1.73 [39]	0	0	0	0
				LDA			
o- $MAPbI_3$	1.52	0.64	1.65 [37]	0	0	0	0
t- $MAPbI_3$	1.38	0.61	1.61 [37]	17	8	0.025	0.019
pc- $MAPbI_3$	1.52	0.50	1.63 [38]	98	36	0.054	0.050
pc- $FAPbI_3$	1.25	0.23	1.52 [37]	20	1	0.020	0.003
pc- $CsPbI_3$	1.56	0.52		96	33	0.056	0.047
c- $CsPbI_3$	1.18	0.10	1.73 [39]	0	0	0	0

that similar behavior is present. Both organic and inorganic finite-temperature structures exhibit significant band splitting. The soft polar nature of halide perovskites leads to large distortions and resulting asymmetry at heavy atom sites. With Pb-based perovskites, this result in particularly pronounced spin splittings. We correlate a metric relevant for device physics (spin-split bands) directly with features that can be observed (lattice distortion).

II. COMPUTATIONAL METHODS

The electronic structure of lead halide perovskites is sensitive to the choice of Hamiltonian. Relativistic effects lower and split the atomic levels of Pb and I (Table S1). These effects carry over into the condensed phase, resulting in a large renormalization of the band gap (Table I). There is in addition a k-dependent contribution originating from local asymmetry and spin-orbit coupling, which gives rise to the aforementioned spin splitting. In these materials, the quasiparticle corrections are large, which necessitates going beyond Kohn-Sham density-functional theory (DFT) [13,30,31]. Here we use relativistic quasiparticle *GW* theory (QS*GW*), as implemented in the all-electron QUESTAAL [32] software package. For its greater computational efficiency, we also use the local density approximation (LDA) [33]. Further computational details, along with a discussion of the accuracy of QS*GW*, are provided as Supplemental Material (SM) [34].

III. RESULTS

A. Static crystal structure representations

As an initial reference we study static geometry-relaxed crystal structures [35]. Our calculated QS*GW* band structures of $CH_3NH_3PbI_3$ in three phases are shown in Fig. 1. The low-temperature orthorhombic (D_{2h} point group) phase has a conventional-looking band structure with a direct band gap. The principal effect of SOC (compare dashed gray and colored lines) is a renormalization of the conduction band energy by circa 0.8 eV (compare Table I to atomic splitting, Table SM-S1).

The center of inversion present in the orthorhombic phase of $CH_3NH_3PbI_3$ is lost in static representations of the tetragonal and cubic phases. There is now a shift of the band extrema away from the high-symmetry points: Spin splitting is activated. The indirect band gaps are 2.00 eV and 1.87 eV for the tetragonal

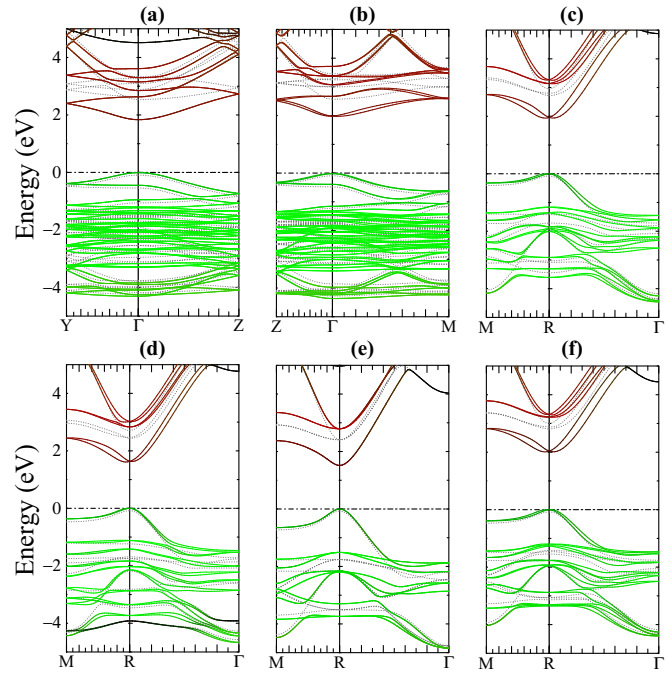

FIG. 1. Relativistic QS*GW* band structures. $CH_3NH_3PbI_3$ in its (a) orthorhombic, (b) tetragonal, and (c) pseudocubic phases. $HC(NH_2)_2PbI_3$ in a (d) pseudocubic structure and $CsPbI_3$ in (e) cubic and (f) pseudocubic structures. Bands are colored based on a Mulliken projection: Pb p states are highlighted in red and I p states in green. Partial density of states are provided in Fig. S1.

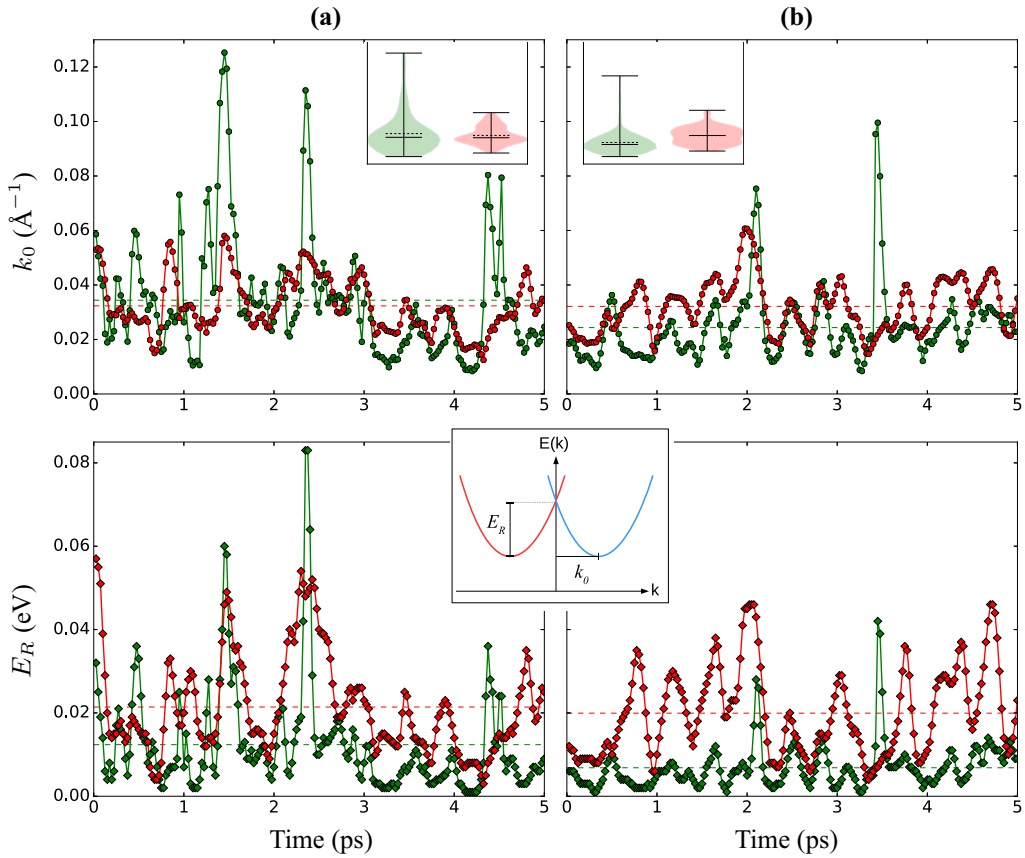

FIG. 2. Magnitude of momentum and energy offsets in the valence and conduction bands for (a) $CH_3NH_3PbI_3$ and (b) $CsPbI_3$ from 200 frames of *ab initio* molecular dynamics. VB splittings are plotted in green, CB in red, and average splittings as dashed lines. The schematic highlights the spin-splitting parameters E_R and k_0. The probability densities of the momentum offsets are represented by violin plots, where the mean and median values are shown as dashed and solid lines.

and pseudocubic phases, and conduction-band minima are offset by 0.03 Å^{-1} and 0.06 Å^{-1} from high symmetry points. The latter calculated value is a giant spin splitting, comparable in magnitude to the largest values experimentally observed in bulk systems [36]. These band splitting features are consistent with the electron-hole recombination kinetics observed in experiment. In particular, there is a sharp fall off in the charge carrier lifetime at the transition to the orthorhombic phase, where a direct gap is recovered [20,22].

The inversion-asymmetric tetragonal and pseudocubic structures have a Rashba-like spin splitting, with the usual k-linear dispersion relation and helical spin texture [14,17,29]. However, instead of a ring of extrema that is typically observed in Rashba materials, here there are two distinct extremal points. As previously shown [13], the extremal points are antipodal to each other, with a connecting path that passes through two saddle points. At the DFT level, the conduction and valence bands have approximately the same momentum offset k_0 (difference in momentum between high-symmetry point and extremal point). However, QS*GW* results show that k_0 in the valence band (VB) is roughly half that of the conduction band (CB). Relative to QS*GW*, LDA-DFT also overestimates the energy offset E_R (defined as the difference in energy between the spin-split extremal point and high-symmetry point) in both bands, see Table I.

A central question is to what extent the calculated spin splitting depends on the choice of cation. The methylammonium cation has a large built-in dipole [40], which by itself applies a local electric field to the lead-iodide octahedra. Another common organic cation, formamidinium [$HC(NH_2)_2$ or FA], possesses a much smaller dipole [40] but still breaks the inversion symmetry of the unit cell and applies steric distortion to the octahedra [Fig.1(d)]. On the other hand, the inorganic cation in $CsPbI_3$ has spherical symmetry and there is no built-in dipole. The room-temperature phase is often assumed to be cubic (O_h point group), with a direct gap [see Fig. 1(e)].

We consider these cations in a range of structures (Table I with band structures in Fig. 1). Universally, once inversion symmetry is broken, a similar band splitting is observed. The cation dipole does not appear to directly affect the band splitting. Instead, the cations are found to play an indirect role by influencing the lead-iodide octahedral distortions through steric effects; it is these structural distortions that generate the spin splitting. In the case of Cs, the ideal cubic structure has no spin splitting. If we substitute Cs for methylammonium in the pseudocubic structure, and energy minimize with respect to Cs while keeping Pb and I fixed, then an almost identical spin splitting is generated [see Fig. 1(f)].

In contrast to the average (long-range) cubic structure inferred from Bragg diffraction, recent measurements suggest that the structure of $CsPbI_3$ is locally symmetry broken at

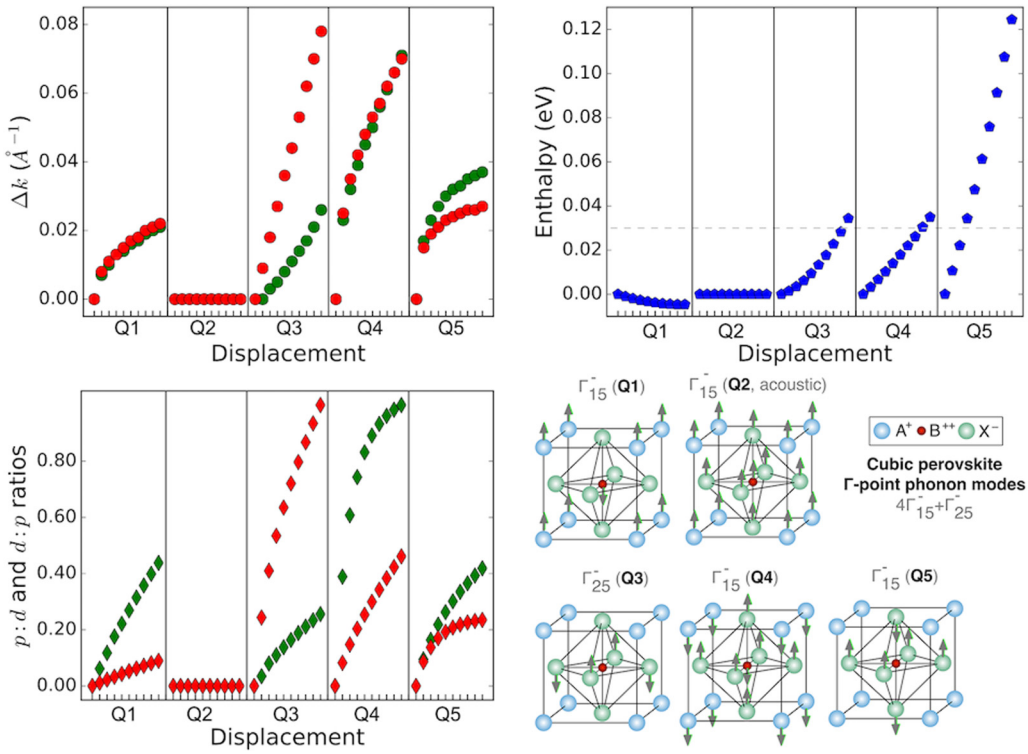

FIG. 3. Analysis of the zone-center phonon modes for cubic $CsPbI_3$. The effect of displacement along each mode (Q) is shown for: momentum offsets (k_0) in the VB (green) and CB (red); enthalpy change relative to reference cubic structure (k_BT at 300 K is plotted as a dashed gray line); ratio of $d:p$-character (green) in the VB maximum and $p:d$-character (red) in the CB minimum versus displacement. The ratios are computed from Mulliken populations and both sets are normalized for comparison. Corresponding changes in effective masses and density of states are shown in Table S2 and Fig. S7.

room temperature [41–43]. Polar fluctuations have recently been observed in a number of other perovskites [44]. Thermal disorder is expected to be necessary to understand the nature of the spin splitting.

B. Dynamic disorder at finite temperatures

We consider a thermodynamic ensemble of structures from *ab initio* MD at 300 K and calculate the electronic structure at the LDA level (all electron with spin-orbit coupling). The LDA tends to predict k_0 values that are in close agreement with QS*GW* in the CB but overestimated in the VB, while E_R tends to be overestimated in both bands (further details are provided in the SM [34]). We consider $2 \times 2 \times 2$ supercell expansions of the $MAPbI_3$ and $CsPbI_3$ unit cells, allowing for zone boundary tilting modes. After an initial equilibration period, we sample 200 consecutive frames, each separated by 0.025 ps. This time discretization is intentionally chosen to be less than the characteristic motion of the material (e.g., the 2 ps methylammonium rotation and associated cage distortion). We can track how the electronic structure and spin splitting evolve in time.

For both materials the momentum offset k_0 in the conduction band (Fig. 2) fluctuates around a value of $0.03\,\text{Å}^{-1}$. A similar picture is seen for the energy offsets, with averages around 20 meV. The MA cation results in more variable behavior, particularly in the VB, as evidenced by the larger spread (and broader distribution) in the inset violin plots. This is in line with the dominant contributions to the valence band coming from the lighter iodine atoms. Interestingly, the Cs cation, despite having the same average, results in a broader distribution in the conduction band. The splittings are reduced relative to the single cells but, crucially, are nonzero throughout. As well as k_0 changing in magnitude, the band extrema rotate relative to one another (see Figs. S2 and S3). The average angle is 44° for $MAPbI_3$ and 38° for $CsPbI_3$ (relative angles are as high as 90°). The spin is locked to the momentum and its polarization is also found to fluctuate in time (see Figs. S4 and S5).

The similar band splittings observed for both cations suggest that the dominant contribution is thermal distortion of the inorganic cage. A Fourier transform of the time series shows that the spin splitting has the same periodicity as low frequency phonon modes (Fig. S6). These modes are distortions of the octahedral cage and associated rotations of the organic cation in the case of $MAPbI_3$. As such, spin splitting is expected to be present at room temperature for all lead iodide perovskites, independent of cation or (long-range) crystal symmetry.

$CsPbI_3$ is a striking example of the importance of finite-temperature lattice dynamics on the electronic structure. A static calculation predicts no spin splitting. Such a cubic unit cell agrees with the average structure determined from x-ray diffraction [45]; however, this phase has a number of vibrational instabilities that give rise to dynamic distortions [46]. At any point in time, the lattice distortions break the local symmetry, give rise to local fields, and produce spin splitting.

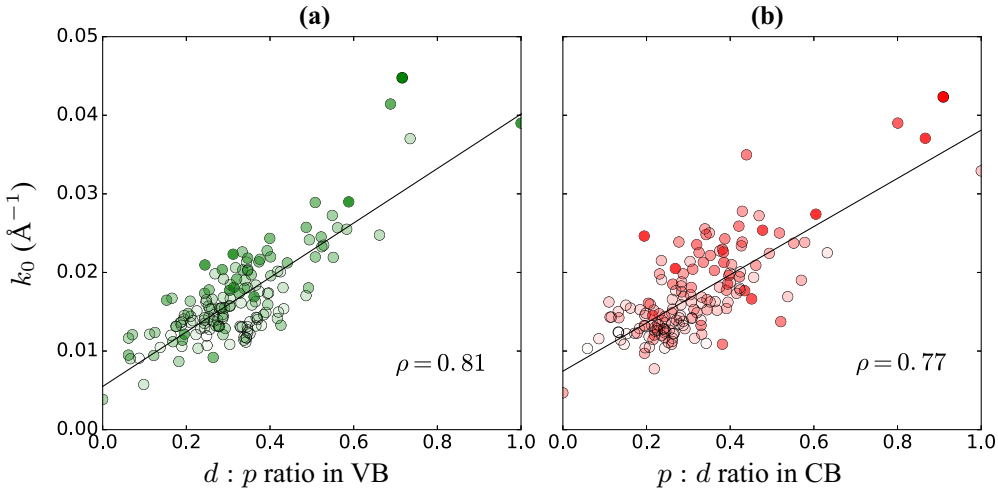

FIG. 4. Magnitude of momentum offset k_0 versus (a) $d : p$ ratio in the VB and (b) $p : d$ ratio in the CB for 147 MA orientations in $MAPbI_3$. The total energy of each structure is represented by the opacity level of the marker face color, where higher opacity refers to higher energy. The Pearson correlation coefficient (ρ) between the splitting and ratio magnitudes is also shown.

To better understand the structural origins of the splitting, we return to a unit cell representation and follow symmetry breaking by phonon modes. In the frozen-phonon approximation, we separately distort along each Γ-point normal mode and track k_0. The magnitude of these distortions are chosen (from the phonon frequency) to sample a thermodynamic degree of freedom to an energy of k_BT (300 K).

The five unique cubic-perovskite phonon modes are depicted in Fig. 3. The acoustic mode (Q2) is a rigid translation of the lattice and does not change the energy or electronic structure; it is included as a cross validation. Each other mode results in a monotonic spin splitting as a function of displacement. The first mode is soft for $CsPbI_3$, corresponding to 'rattling' of the Cs and Pb ions. The dependence of k_0 on displacement has the same form for both VB and CB. Notable differences in k_0 are observed in both bands for Q3 and Q5. The largest splittings are found in modes Q3 and Q4. In Q4, the Pb atom moves off site; it also has the largest initial (low displacement, low energy) splitting. Mode Q3 is composed of octahedral twisting (iodine motion) around Pb. It shows remarkably linear splitting as a function of distortion and there are considerably larger splittings in the conduction band than in the valence band.

Spin-orbit coupling is commonly considered a local effect, significant around heavy atoms such as Pb (Z = 82) and I (Z = 53). The spin splitting has its origins in spin-orbit coupling, which appears as a correction in in the nonrelativistic limit of the Dirac equation:

$$H_{\mathrm{SOC}} = \frac{2}{c^2}(\nabla V \times \mathbf{p}) \cdot \mathbf{s}.$$

Spin splitting is a result of local asymmetry in both the potential and the wave function (through the momentum operator) in the core regions of heavy nuclei; a large splitting requires a large value for both [47–49].

The asymmetry of the wave function can be estimated by the ratio of the l to $l \pm 1$ angular-momentum character (providing an effective gradient) in a region close to the nuclear core [47]. The decomposition in Fig. 3 is based on a Mulliken analysis, which does not project out small regions close to the nuclei; nevertheless, the ratios correlate closely to the observed shifts in k_0. As an example, the p and d ratios are shown but there is a dependence on the choice of l to $l \pm 1$ character (p and s ratios are provided in Fig. S8, further details are provided in the SM). The spin splitting is also found to have a dependence, though weaker, on local electric fields (see Fig. S9). The angle between the electric field and vector k_0 is approximately $90 \pm 2^\circ$ in each case, in line with the perpendicular relation in the Rashba model. The local symmetry breaking can be seen through changes in the charge density (Fig. S10).

To quantify the correlation for disordered structures, we consider 147 random methylammonium orientations where the PbI_3 network is locally relaxed around each configuration. Optimized structures with energy $> k_BT$ were excluded. The $d : p$ and $p : d$ ratios are found to correlate well with the magnitude of the momentum offset k_0 (see Fig. 4). Improved agreement is expected by accounting for different l to $l \pm 1$ ratios and only considering regions close to the nuclear cores. The splitting is also found to correlate with the magnitude of the local electric field (Fig. S11).

In addition to band splitting, structural distortions generally widen the band gap (Fig. 5) and flatten the frontier bands (Fig. S7). QS*GW* generally *overestimates* band gaps [50] but *underestimates* the band gap in $CsPbI_3$ in the cubic structure. However, QS*GW* predicts an increase of 0.44 eV in the pseudocubic structure (Table I), improving agreement with room temperature experiments. Average $MAPbI_3$ and $CsPbI_3$ band gaps from MD simulations also increase by 0.25 and 0.73 eV relative to athermal structures, and they increase for $CsPbI_3$ phonon mode displacements (Fig. 5). These trends originate from the antibonding character of the frontier bands [51] and a reduction in spin-orbit splitting of the CB originating from a reduction in Pb-p content. Both trends are demonstrated through an analysis of the shifts in the band edges with displacements along the normal modes (Fig. 5). There is a general tendency for the VB to be pushed *down* and for the CB to be pushed *up*, though how each edge shifts depends on the normal mode. The VB downshift is in line with a reduction in antibonding between I-p and Pb-s states [51].

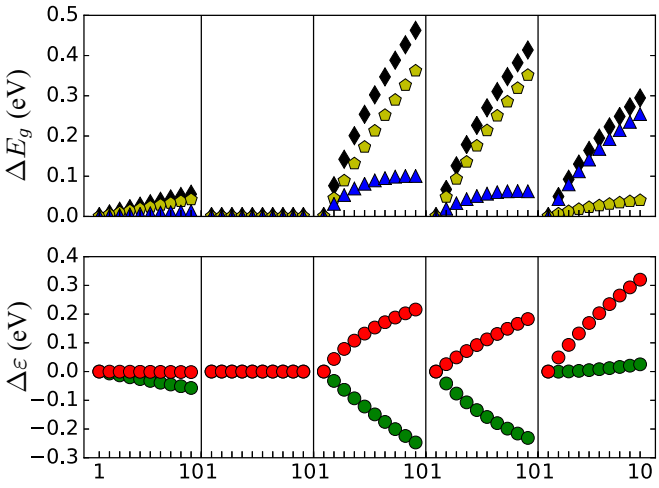

FIG. 5. Top: band-gap change ΔE_g, relative to the undistorted cubic case, for displacements along a normal mode. The total change with SOC is shown in black, change without SOC (scalar relativistic) is shown in yellow, and change due to SOC (difference between total and scalar relativistic changes) is shown in blue. Bottom: change in extremal point eigenvalues, relative to the cubic case, for displacements along a normal mode. VBM change is shown in green and CBM change is shown in red. Band alignment details are provided in the SM.

The largest VB shifts are seen for modes 3 (I motion around Pb) and 4 (Pb off-centering). The band-gap shifts in modes 3 and 4 are predominantly due to scalar relativistic changes (yellow markers in Fig. 5). On the other hand, the CB upshift correlates closely with a reduction in Pb-p character, largely a result of reduced SO coupling. As evidenced in Fig. S12, the larger CB shifts in modes 3, 4, and 5 coincide with significant reductions in Pb-p character. This effect is clearly seen in mode 5 where there is a large upshift in the CB but negligible change in the VB: The resulting band-gap shift is dominated by changes in the SO coupling (blue markers in Fig. 5). Further computational details are provided in the SM.

IV. CONCLUSIONS

A spin-split indirect gap has been found in thermal ensembles of organic-inorganic and inorganic lead halide perovskites. The splitting arises due to spin-orbit coupling in the presence of local asymmetry, which we relate to distortions in the lead iodide framework. The role of the perovskite A-site cation appears to be steric in nature. The asymmetry in the electronic wave function and, to a lesser extent, the local electric field were found to correlate well with the magnitude of the momentum offset. Overall, structural distortions lead to spin-split bands and a widening of the band gap. This provides a method to go from an observed (temperature-dependent) disorder measure to a measure of the indirect gap. Temperature-dependent observations of the band character will provide information to confirm these hypotheses.

ACKNOWLEDGMENTS

Support has been received from the EPSRC (EP/M009580/1, EP/M011631/1, and EP/K016288/1). For computational resources, we were supported by the ARCHER UK National Supercomputing Service and the UK Materials and Molecular Modelling Hub for computational resources (EPSRC Grant No. EP/P020194/1).

[1] R. Elliott, Phys. Rev. **96**, 280 (1954).
[2] R. Winkler, *Spin-Orbit Coupling Effects in Two-Dimensional Electron and Hole Systems* (Springer, Berlin, 2003).
[3] G. Dresselhaus, Phys. Rev. **100**, 580 (1955).
[4] E. Rashba, Sov. Phys. Solid State **1**, 368 (1959).
[5] E. Rashba and V. Sheka, Fiz. Tverd. Teka **2**, 162 (1959).
[6] E. I. Rashba, Sov. Phys. Solid State **2**, 1224 (1960).
[7] G. Bihlmayer, O. Rader, and R. Winkler, New J. Phys. **17**, 050202 (2015).
[8] Y. A. Bychkov and E. Rashba, Pis'ma Zh. Eksp. Teor. Fiz. **39**, 66 (1984) [JETP Lett. **39**, 78 (1984)].
[9] R. Winkler, Phys. Rev. B **69**, 045317 (2004).
[10] X. Zhang, Q. Liu, J.-W. Luo, A. J. Freeman, and A. Zunger, Nat. Phys. **10**, 387 (2014).
[11] I. Žutić, J. Fabian, and S. D. Sarma, Rev. Mod. Phys. **76**, 323 (2004).
[12] J. Fabian, A. Matos-Abiague, C. Ertler, P. Stano, and I. Zutic, Acta Physica Slovaca **57**, 565 (2007).
[13] F. Brivio, K. T. Butler, A. Walsh, and M. van Schilfgaarde, Phys. Rev. B **89**, 155204 (2014).
[14] M. Kim, J. Im, A. J. Freeman, J. Ihm, and H. Jin, P.N.A.S. **111**, 6900 (2014).
[15] A. Amat, E. Mosconi, E. Ronca, C. Quarti, P. Umari, M. K. Nazeeruddin, M. Grätzel, and F. De Angelis, Nano Lett. **14**, 3608 (2014).
[16] C. Motta, F. El-Mellouhi, S. Kais, N. Tabet, F. Alharbi, and S. Sanvito, Nat. Commun. **6**, 7026 (2015).
[17] F. Zheng, L. Z. Tan, S. Liu, and A. M. Rappe, Nano Lett. **15**, 7794 (2015).
[18] T. Etienne, E. Mosconi, and F. De Angelis, J. Phys. Chem. Lett. **7**, 1638 (2016).
[19] L. Z. Tan and A. M. Rappe, arXiv:1708.05436.
[20] E. M. Hutter, M. C. Gélvez-Rueda, A. Osherov, V. Bulović, F. C. Grozema, S. D. Stranks, and T. J. Savenije, Nat. Mater. **16**, 115 (2017).
[21] D. Niesner, M. Wilhelm, I. Levchuk, A. Osvet, S. Shrestha, M. Batentschuk, C. Brabec, and T. Fauster, Phys. Rev. Lett. **117**, 126401 (2016).
[22] T. Wang, B. Daiber, J. M. Frost, S. A. Mann, E. C. Garnett, A. Walsh, and B. Ehrler, Energy Environ. Sci. **10**, 509 (2017).
[23] D. Niesner, M. Hauck, S. Shrestha, I. Levchuk, G. J. Matt, A. Osvet, M. Batentschuk, C. Brabec, H. B. Weber, and T. Fauster, arXiv:1703.08740.
[24] W. S. Yang, B.-W. Park, E. H. Jung, N. J. Jeon, Y. C. Kim, D. U. Lee, S. S. Shin, J. Seo, E. K. Kim, J. H. Noh, and S. I. Seok, Science **356**, 1376 (2017).
[25] A. Kojima, K. Teshima, Y. Shirai, and T. Miyasaka, J. Am. Chem. Soc. **131**, 6050 (2009).
[26] T. M. Brenner, D. A. Egger, L. Kronik, G. Hodes, and D. Cahen, Nat. Rev. Mater. **1**, 15007 (2016).

[27] M. Ahmadi, T. Wu, and B. Hu, Adv. Mater. **29**, 1605242 (2017).
[28] P. Azarhoosh, S. McKechnie, J. M. Frost, A. Walsh, and M. Van Schilfgaarde, APL Mater. **4**, 091501 (2016).
[29] M. Kepenekian, R. Robles, C. Katan, D. Sapori, L. Pedesseau, and J. Even, ACS Nano **9**, 11557 (2015).
[30] P. Umari, E. Mosconi, and F. De Angelis, Sci. Rep. **4**, 4467 (2014).
[31] M. R. Filip and F. Giustino, Phys. Rev. B **90**, 245145 (2014).
[32] http://www.questaal.org. Our *GW* implementation was adapted from the original ecalj package, now at https://github.com/tkotani/ecalj/.
[33] W. Kohn and L. J. Sham, Phys. Rev. **140**, A1133 (1965).
[34] See Supplemental Material at http://link.aps.org/supplemental/10.1103/PhysRevB.98.085108 for additional computational details and analysis figures.
[35] F. Brivio, J. M. Frost, J. M. Skelton, A. J. Jackson, O. J. Weber, M. T. Weller, A. R. Goñi, A. M. A. Leguy, P. R. F. Barnes, and A. Walsh, Phys. Rev. B **92**, 144308 (2015).
[36] K. Ishizaka, M. Bahramy, H. Murakawa, M. Sakano, T. Shimojima, T. Sonobe, K. Koizumi, S. Shin, H. Miyahara, A. Kimura *et al.*, Nat. Mater. **10**, 521 (2011).
[37] K. Galkowski, A. Mitioglu, A. Miyata, P. Plochocka, O. Portugall, G. E. Eperon, J. T.-W. Wang, T. Stergiopoulos, S. D. Stranks, H. J. Snaith *et al.*, Energy Environ. Sci. **9**, 962 (2016).
[38] C. Quarti, E. Mosconi, J. M. Ball, V. D'Innocenzo, C. Tao, S. Pathak, H. J. Snaith, A. Petrozza, and F. De Angelis, Energy Environ. Sci. **9**, 155 (2016).
[39] G. E. Eperon, G. M. Paternò, R. J. Sutton, A. Zampetti, A. A. Haghighirad, F. Cacialli, and H. J. Snaith, J. Mater. Chem. A **3**, 19688 (2015).
[40] J. M. Frost, K. T. Butler, F. Brivio, C. H. Hendon, M. Van Schilfgaarde, and A. Walsh, Nano Lett. **14**, 2584 (2014).
[41] F. Bertolotti, L. Protesescu, M. V. Kovalenko, S. Yakunin, A. Cervellino, S. J. Billinge, M. W. Terban, J. S. Pedersen, N. Masciocchi, and A. Guagliardi, ACS nano **11**, 3819 (2017).
[42] O. Yaffe, Y. Guo, L. Z. Tan, D. A. Egger, T. Hull, C. C. Stoumpos, F. Zheng, T. F. Heinz, L. Kronik, M. G. Kanatzidis, J. S. Owen, A. M. Rappe, M. A. Pimenta, and L. E. Brus, Phys. Rev. Lett. **118**, 136001 (2017).
[43] M. Isarov, L. Z. Tan, M. I. Bodnarchuk, M. V. Kovalenko, A. M. Rappe, and E. Lifshitz, Nano Lett. **17**, 5020 (2017).
[44] P. Guo, Y. Xia, J. Gong, C. C. Stoumpos, K. M. McCall, G. C. Alexander, Z. Ma, H. Zhou, D. J. Gosztola, J. B. Ketterson *et al.*, ACS Energy Lett. **2**, 2463 (2017).
[45] C. K. Møller, Nature (London) **182**, 1436 (1958).
[46] R. X. Yang, J. M. Skelton, L. da Silva, J. M. Frost, and A. Walsh, J. Phys. Chem. Lett. **8**, 4720 (2017).
[47] G. Bihlmayer, Y. M. Koroteev, P. Echenique, E. Chulkov, and S. Blügel, Surf. Sci. **600**, 3888 (2006).
[48] M. Nagano, A. Kodama, T. Shishidou, and T. Oguchi, J. Phys.: Condens. Matter **21**, 064239 (2009).
[49] S. Abdelouahed and J. Henk, Phys. Rev. B **82**, 193411 (2010).
[50] M. van Schilfgaarde, T. Kotani, and S. Faleev, Phys. Rev. Lett. **96**, 226402 (2006).
[51] L.-Y. Huang and W. R. L. Lambrecht, Phys. Rev. B **88**, 165203 (2013).